Supporting Information

Revealing How Internal Sensors in a Smart Battery Impact the Local Graphite Lithiation Mechanism

Annabel Olgo[1], Sylvie Genies[2], Romain Franchi[2], Cédric Septet[2], Quentin Jacquet[1], Quentin Berrod[1], Rasmus Palm[3], Pascale Chenevier[1], Elise Villemin[2], Claire Villevieille[4], Nils Blanc[5], Samuel Tardif[6], Olivier Raccurt[2*], and Sandrine Lyonnard[1*]

[1] Univ. Grenoble Alpes, CEA, CNRS, Grenoble INP, IRIG, SyMMES, 38000 Grenoble, France

[2] Univ. Grenoble Alpes, CEA, LITEN, DEHT, 38000 Grenoble, France

[3] Univ. Tartu, Institute of Chemistry, 50411, Tartu, Estonia

[4] Univ. Grenoble Alpes, Univ. Savoie Mont Blanc, CNRS, Grenoble INP, LEPMI, 38000 Grenoble, France

[5] Univ. Grenoble Alpes, CNRS, Inst. NEEL, 38054, Grenoble, France

[6] Univ. Grenoble Alpes, CEA, IRIG, MEM, 38000 Grenoble, France

Corresponding authors: olivier.raccurt@cea.fr and sandrine.lyonnard@cea.fr

1 Sensors

Characteristics of the optical fiber sensor: A detailed description of the optical sensor was previously published by E. Villemin *et al.*[1]. Fig. S1a shows the composition and dimensions of the optical sensor. The optical fiber sensor was prepared by depositing Gd_2O_2S: Er^{3+}, Yb^{3+} microparticles at the end of the optical fiber embedded in a silica sol-gel coating covered by a PMMA coating to protect the silica. Before depositing the optical probe the Tefzel coating was removed at a distance of 10 cm. The diameter of the fiber inserted in the pouch cell was 225 µm. Fig. S1b–d gives a schematic view of the thickness of each layer in the cells (electrodes, collectors, and separator), the optical fiber diameter, and the impact of fiber inserted between the positive electrode and separator.

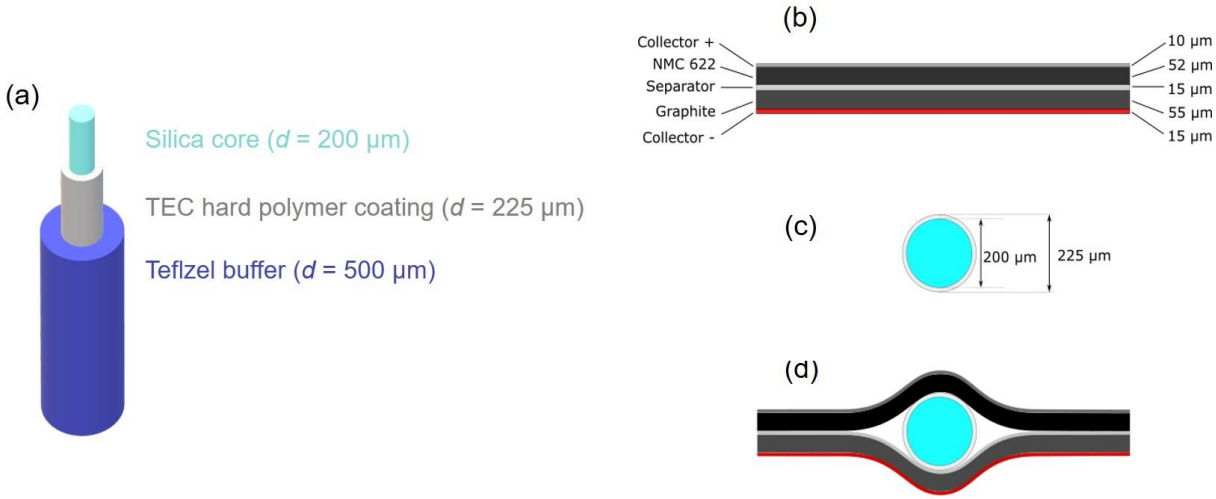

Figure S1. **(a)** Composition and dimension of the optical fiber FT200EMT. **(b)** Dimensions of one unit cell stack, **(c)** Dimensions of the optical fiber, **(d)** Impact of the fiber dimensions on the deformation of electrode+separator layers.

Characteristics of the reference electrode sensor: The reference electrode ($(Li_{(1-x)})FePO_4/LiFeO_4$, E = 3.424 V *vs* Li^+/Li) was made by deposing a thin layer of gold on a separator foil and coating it with LFP ink (Fig. S2). The dimensions of the reference electrode are detailed in Table S1.

Table S1: Dimensions of the reference electrode, where S is the surface area of components and $S_{separator}$ is the surface area of an additional piece of a separator.

	Thickness (µm)	***S* (cm²)**	**$S_{separator}$ (cm²)**
Separator foil	25		
Gold coating	0.15	0.36 (square : 6 x 6 mm)	0.64 (square : 8 x 8 mm)
LFP coating	35		
Total	~ 60		

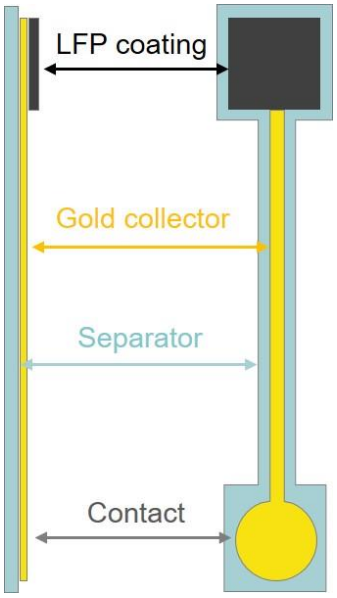

Figure S2. Schematic view of the reference electrode.

2 Electrochemical cells and materials

Two cell designs were characterized *operando* by electrochemistry and WAXS analyses. The electrical characteristics of the internal components of both cell designs are given in Table S2.

Table S2: Positive and negative electrode characteristics.

Positive electrode (pristine state)	
Material	NMC622
Active material loading (%)	96.4
Press density (g/cc)	3.30
Coating weight (mg/cm²/side)	16.7
Coating thickness (µm/side)	55
Collector thickness (µm)	15
Negative electrode (pristine state)	
Material	Graphite
Active material loading (%)	94.8
Press density (g/cc)	1.8
Coating weight (mg/cm²)	10
Coating thickness (µm/side)	52
Collector thickness (µm)	8
Separator	
Material	PE with Al_2O_3 coating on the NMC side
Thickness µm	15 µm

Preparation and characteristics of the instrumented commercial multi-layered cell. The commercial prismatic pouch cells (1.1 Ah) were obtained from Li-Fun Technology in a non-activated state (Fig S3a). The casing was dismounted and the jellyroll was unfolded (Fig. S3b and S4). The optical fiber and reference electrode were inserted in the center of the rolling electrode between the separator and NMC622 electrode (Fig S3b). Sensors (optical fiber and reference electrode) were placed on the separator and fixed with a small piece of Kapton tape. A small piece of separator was placed over the reference electrode to ensure electrical isolation between the reference electrode and the NMC622 electrode. The reference electrode $LiFePO_4$ (LFP)-based coating was positioned in front of the graphite electrode. The jellyroll was then rewound and the cell was activated by adding liquid organic electrolyte.

Figure S3. The procedure of inserting sensors into a commercial cell. **(a)** Non-activated commercial cell obtained from Li-FUN technology; **(b)** Disassembled cell equipped with the optical fiber and reference electrode sensors; **(c)** Rewound cell.

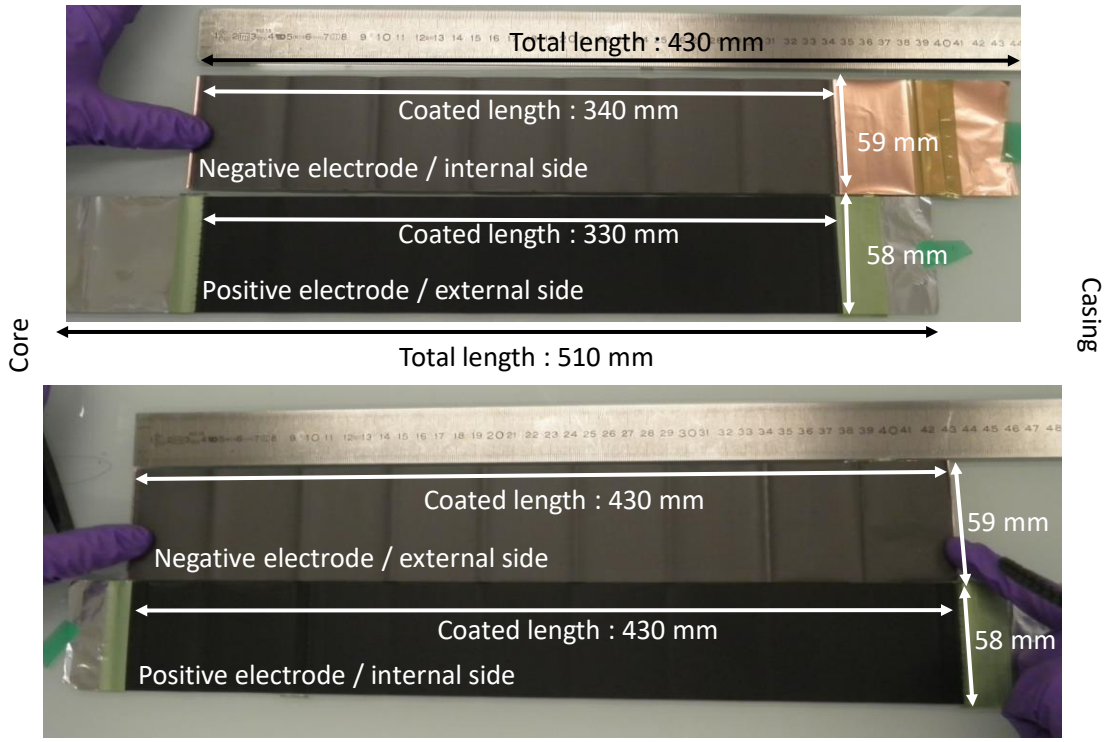

Figure S4. Unwound electrodes of a Li-FUN cell with dimensional measurement and number-of-turns.

Preparation and characteristics of the single layer cell. The single-layer cell was prepared in the lab with a defined protocol ensuring the best design to obtain a reference battery cell composed of one graphite and one NMC622 electrode layer. This single-layer cell was re-assembled by using pristine electrodes from a Li-Fun cell after removing the coating from one side (Fig. S5). Practically, double-side coated electrodes were taped around the edge before removing the coating from the top with *N*-methyl pyrrolidone-impregnated or water-impregnated paper for positive and negative electrodes. The cell characteristics are reported in Table S3.

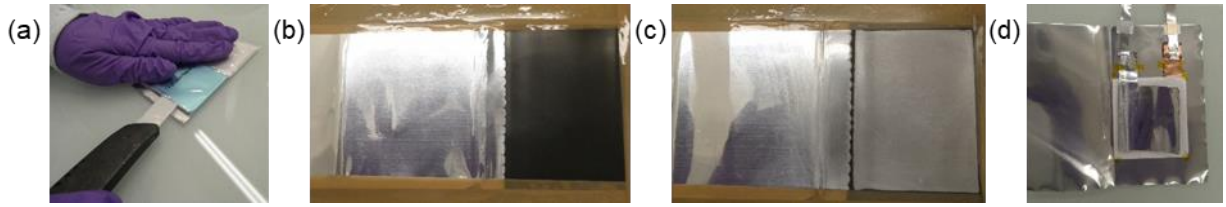

Figure S5. The procedure for obtaining the reference single-layer cell. First, the commercial non-activated cell was opened and disassembled. The coating was removed from one side while protecting the other side by taping the electrode around the edge **(a)**. **(b)** Before and **(c)** after removing the coating from one side of the electrode; (d) Assembled single-layer cell.

Table S3: The electrochemical characteristics of the commercial cell multi-layered cell and single-layer cell.

Electrochemical characteristics		
	Multi-layered cell (double-coated electrode)	**Single-layer cell (single-coated electrode)**
Voltage range (V)	3.0–4.2	
Average voltage (V)	3.7@RT,0.2 C	
Optimal capacity (mAh)	1100 mAh@RT,0.2 C	24.5 mAh@RT,0.2 C
Positive real capacity (mAh/cm²)	2.8	
Energy density (Wh)	4.1	0.1
Energy density (Wh/kg)	214	/
Energy density (Wh/L)	425	/
NMC622 area (cm²)	Internal side: 43 x 5.8 cm = 249.4 cm² External side: 33 x 5.8 cm = 191.4 cm²	3.2 x 3.2 cm = 10.24 cm²
Graphite area (cm²)	External side: 43 x 5.9 cm = 253.7 Internal side: 34 x 5.9 cm = 200.6 cm²	3.5 x 3.5 cm = 12.25 cm²

Formation protocol. After sealing the cells, galvanostatic charge-discharge cycling (formation process) was carried out to prepare cells for the *operando* wide-angle X-ray scattering experiment. In Fig. S6 we compare the electrochemical behaviour of the instrumented cell (with sensors) to a reference cell (with no sensors inside) after the formation (see Table S4 for characteristics). The electrochemical performance of the cells is comparable, with a limited loss of capacity in the instrumented cell, ~0.1 Ah (Table S5). This value is compatible with the amount of inactive area masked by both the reference electrode and fiber. Regarding the reference electrode, we estimated that the surface masked by the electrode (0.36 cm^2) results in an equivalent size of inactive area. The masked surface for the optical fiber was estimated by considering that the width of the non-active surface is equal to twice the fiber diameter, i.e. 0.5 cm^2.

Tabel S4. Formation protocol for the multi-layered and single-layer cell at laboratory conditions, temperature 25°C.

Formation protocol		
Cycle	**Process**	**Value**
0	Rest	2 h
1	CC Charge	C/10, U_{Limit} = = 2.7 V
	CV Charge	4.2 V for 3 h
	CC Discharge	C/10, U_{Limit} = 2.5 V
	Rest	5 h
2 – 4	CC Charge	C/2, U_{Limit} = 4.2 V
	CV Charge	4.2 V for 3 h
	Rest	5 min
	CC Discharge	C/2, U_{Limit} = 2.8 V
	Rest	5 min

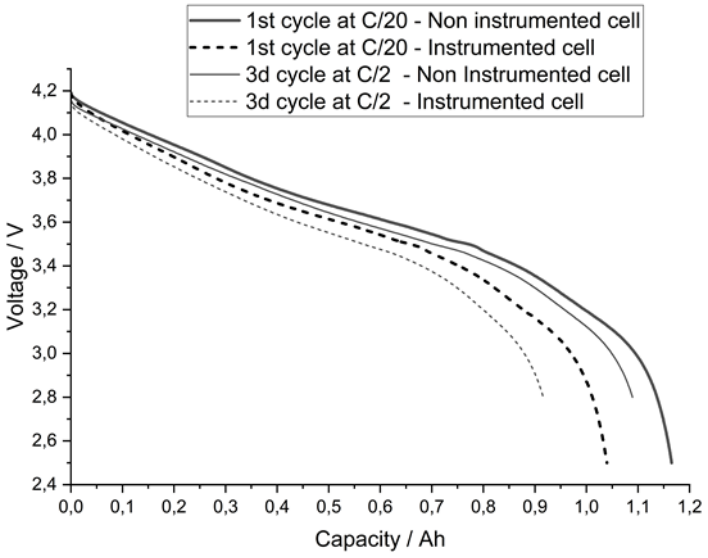

Figure S6: Discharge profiles of the multi-layered cell at C/20 rate (1st cycle) and at C/2 rate (last cycle) obtained during the formation test.

Table S5. Electrochemical data of the cells obtained during the formation cycles.

Single-layer cell (non-instrumented cell)					
Cycle	**Charge (Ah)**	**Discharge (Ah)**	**Charge (Ah/cm²)**	**Discharge (Ah/cm²)**	**%irr (1st cycle)**
1	1.3942	1.1653	0.1323	0.1106	16.4%
2	1.1877	1.1113	0.1127	0.1054	
3	1.1162	1.0993	0.1059	0.1043	
4	1.1025	1.0892	0.1046	0.1033	
Multi-layered cell (instrumented cell)					
Cycle	**Charge (Ah)**	**Discharge (Ah)**	**Charge (Ah/cm²)**	**Discharge (Ah/cm²)**	**%irr (1st cycle)**
1	1.3114	1.0397	0.143	0.113	20.717%
2	1.0528	0.9364	0.115	0.102	
3	0.9518	0.9239	0.104	0.101	
4	0.9363	0.9161	0.102	0.100	

*Surface area (positive electrode) = 10.54 cm²

**Surface area (positive electrode) = 10.54 – (0.36 + 0.5) =10.18 cm² (0.36 cm² is the area masked by the reference electrode, and the impact of the fiber is estimated at 0.5 cm²).

3 *Operando* wide-angle X-ray scattering (WAXS) experiment

Table S6. Electrochemical cycling protocol used during the *operando* WAXS experiment. The test was performed at ambient temperature (25°C).

Galvanostatic charge-discharge protocol			
Cycle	**C-Rate**	**Process**	**Characteristics**
0		Rest	5 min
	C/3	CC discharge	U_{Limit} = 2.8 V
1	C/5	CC Charge	U_{Limit} = 4.2 V
		CV Charge	4.2 V for 1h, $I \leq$ C/20
	C/5	CC Discharge	U_{Limit} = 2.8 V
		Rest	30 min
2	C/2	CC Charge	U_{Limit} = 4.2 V
		CV Charge	4.2 V for 1h, $I \leq$ C/20
		Rest	30 min
	4C	CC Discharge	U_{Limit} = 2.8 V
		Rest	1 h
	C/5	CC Discharge	U_{Limit} = 2.8 V
		Rest	30 min
3 – 5	2C	CC charge	U_{Limit} = 4.2 V
		CV charge	4.2 V for 2h, I ≤ C/20
		Rest	30 min
	4C	CC discharge	U_{Limit} = 2.8 V
		Rest	1 h
	C/2	CC discharge	U_{Limit} = 2.8 V
		Rest	30 min
6	1C	CC charge	U_{Limit} = 4.2 V
		CV charge	4.2 V for 2h, I ≤ C/20
		Rest	30 min
	C/5	CC discharge	U_{Limit} = 2.8 V
		Rest	30 min

3.1 The principle and results of the single-layer cell *operando* WAXS experiment

3x3 grid measurement of the single-layer cell: The aim of the 3x3 grid measurement was to understand if the lithiation of graphite is homogeneous over the entire electrode. During the 3x3 grid measurement, diffraction patterns were collected at nine different scanning points within a hole drilled into a metal plate at the center of the cell. The scanning order of the points was 1→2→3→4→5→6→7→8→9 and the counting time (ct) per point was 30 seconds (Fig. S7).

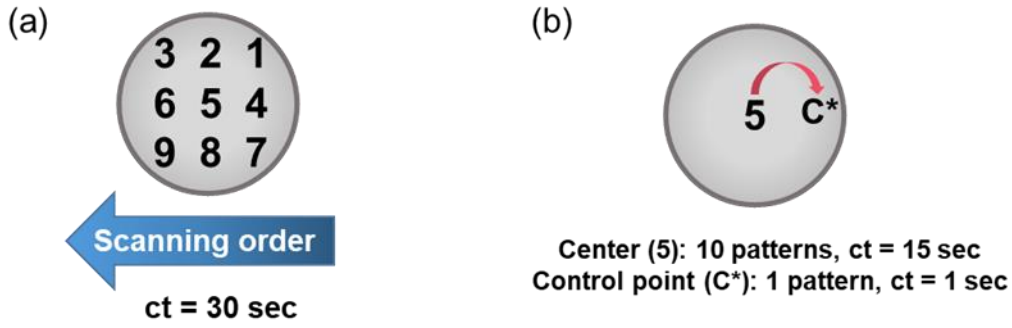

Figure S7. Scanning order (**a**) within a hole during the multi-layered cell and single-layer cell 3x3 grid measurements, (**b)** while measuring continuously the center of a hole in the single-layer cell after 3x3 grid measurement.

Lithiation mechanism of the single-layer cell graphite electrode: During the intercalation of Li-ions into graphite (charging), graphite undergoes a sequence of Li_xC_6 phase transitions, known as the staging of graphite[2]. Different lithiation stages of graphite are referred to as stage *n* (*n* = 1L, 4L, 3L, 2L, 2, and 1), where *n* corresponds to the number of graphene sheets between two interlayer spaces containing Li-ions. The exact stoichiometry at lower lithiation stages (1L, 2L, 3L) is still under debate, due to their lack of in-plane order, and are assumed to have liquid (L)-like behaviour (disordered) within an interslab. Only the stoichiometry of stages 2 and 1 (LiC_{12} and LiC_6, respectively) is known[2–4]. At the beginning of the first cycle, the graphite electrode was in a fully discharged state (Fig. S10). The initial stage transition from graphite to 4L emerged as soon as a positive current was applied and is evident between 2.8–3.55 V. It was followed by a sequence of transition from stage 4L to 3L, biphasic transition from stage 3L to 2 (3.61–3.83 V), and the final transition from stage 2 to 1 (4.00–4.20 V) (Fig. S10). The remaining presence of stage 2 at the end of the voltage hold step is a result of the designed excess capacity in the negative electrode. The delithiation followed a similar path to lithiation with a minor difference of an additional stage transition. Once stage 1 was fully transformed into stage 2, it was followed by the formation of stage 2L instead of 3L. The formation of stage 2L is kinetically slow and rarely observed during the lithiation process, as it involves complex structural reordering between ordered and liquid-like stages[4–6]. In contrast, during delithiation, the transition from stage 2 to 2L requires less structural reorganization, favoring the formation of stage 2L. Based on the fitting results it was found that the (de)lithiation of graphite is homogeneous across different scanning points, with minor variations in phase fractions.

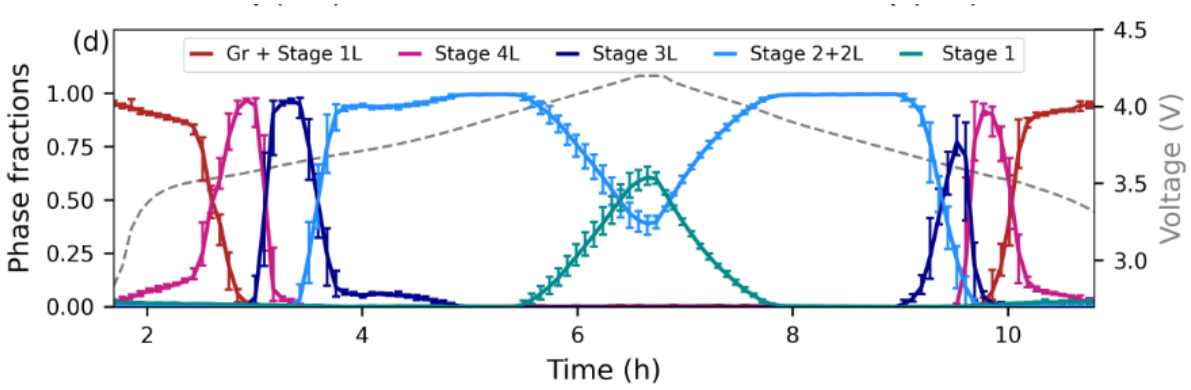

Figure S8. Evolution of averaged phase fractions of different scanning points in time. Error bars demonstrate the maximum and minimum phase fraction values between scanning points.

Beam damage on the single-layer cell graphite electrode: To record structural changes of the single-layer cell graphite electrode at high C-rates, the center of a hole was scanned continuously. For every 10 recorded diffraction patterns (counting time (ct) per diffraction pattern was 15 sec), one diffraction pattern was measured at a control position (ct = 1 sec) to observe the effect of long-term exposure to the synchrotron beam (Fig. S7b). It was observed that graphite lithiation at the center of the hole became more delayed within every cycle, resulting in the coexistence of stages 1L, 3L, 4L, and 2 with graphite mainly in stage 4L (Fig. S9b) at the end of the hold step. This behaviour deviates from previous research findings in this field[6–8].

To gain further insight into this unusual behaviour, diffraction patterns from the control point were analysed. Despite poorer statistics in the collected data compared to the continuously scanned point at the center of the hole, clear contrasts in phase fractions were observed. The control point exhibited more homogeneous stage transitions (Fig. S9c), and the coexistence of different stages while (de)lithiating at higher C-rates align well with the results reported in this field. The significant differences in lithiation mechanisms between the two scanned points suggest that long-term exposure to a synchrotron X-ray beam leads to irreversible changes in the graphite electrode.

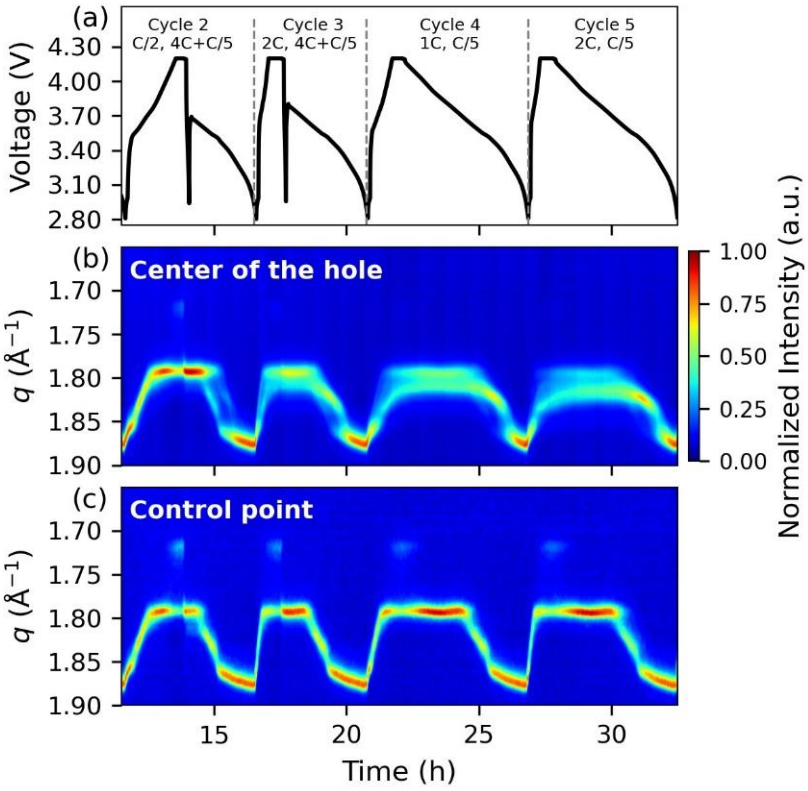

Figure S9. (**a)** Charge-discharge profiles of the single-layer cell obtained after the first cycle. (**b)** 2D plot of the continuously scanned point in the middle of the cell, and (**c)** 2D plot of the diffraction patterns obtained at the control point.

Radiation dose threshold: Understanding when beam damage occurs on an electrode is vital for accurately analysing and interpreting collected data. for the multilayer cell was established as the upper limit for data without beam damage (Fig. S10). In order to estimate beam damage on the graphite electrode, a Python code developed by Thibaut Jousseaume and Samuel Tardif was used to calculate radiation dose and estimate beam damage on the graphite electrode – the code is available in GitHub repository: https://github.com/STardif/dose_estimation. By giving information regarding the cell's components (such as the number and order of electrodes and separators), electrode materials (material, thickness, porosity, etc.), and X-ray beam (size, flux, energy, exposure time), it is possible to estimate the radiation dose and dose rate acquired by each component.

It has been reported that the microstructure of a graphite electrode undergoes modification at radiation doses between 1–4 MGy, and (de)lithiation kinetics are significantly affected beyond 11 MGy[9]. Considering both calculations and the findings discussed earlier, a radiation dose threshold of 1.75 MGy for the multilayer cell was established as the upper limit for data without beam damage (Fig. S10).

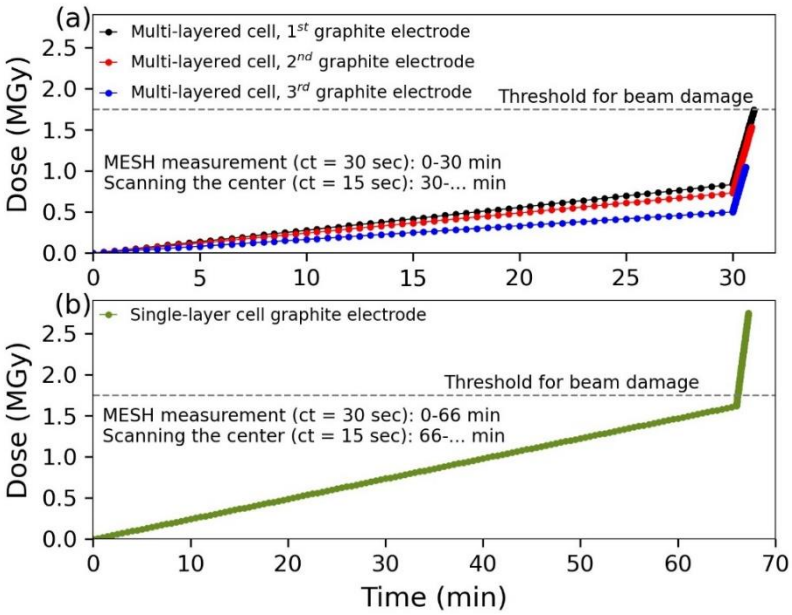

Figure S10. Radiation dose (MGy) evolution in time (min) of (**a)** the three first graphite electrode layers of the multi-layered cell and **(b)** the single-layer cell graphite electrode.

3.2 The principle and results of the multi-layered cell *operando* WAXS experiment

Data acquisition platform. The multi-sensor platform has been developed in the frame of the European project INSTABAT to monitor the usual BMS (voltage, current, temperature) characteristics and integrate measurements from sensors (e.g., thermoluminescence, reference voltage from anode and cathode). The platform is based on a National Instrument PXI computer that manages dual optical and electrochemical signals. A Keysight digital multimeter is used to measure all electrochemical parameters. M970F3 LED (970 nm, 5.9 mW, Thorlabs) was used as an excitation source for the optical fiber. The excitation light was transported through an RP20 (Thorlabs) multimode optical fiber to the sample and collected the light from the sample to the compact CCD spectrometer (CCS, Thorlabs). An achromatic collimator for multimode fibers (F950SMA-A Thorlabs) was used to measure the powder luminescence in the collimator-coupling box. The Biologic VMP3 battery cycler, multi-sensor platform, and X-ray equipment work in parallel. While the cycler applies the defined current profiles, the platform measures the physical parameters of the cell at a configurable period from 1 to 10 seconds. At the same time, diffraction patterns are recorded at time steps dependent on their location and integration time.

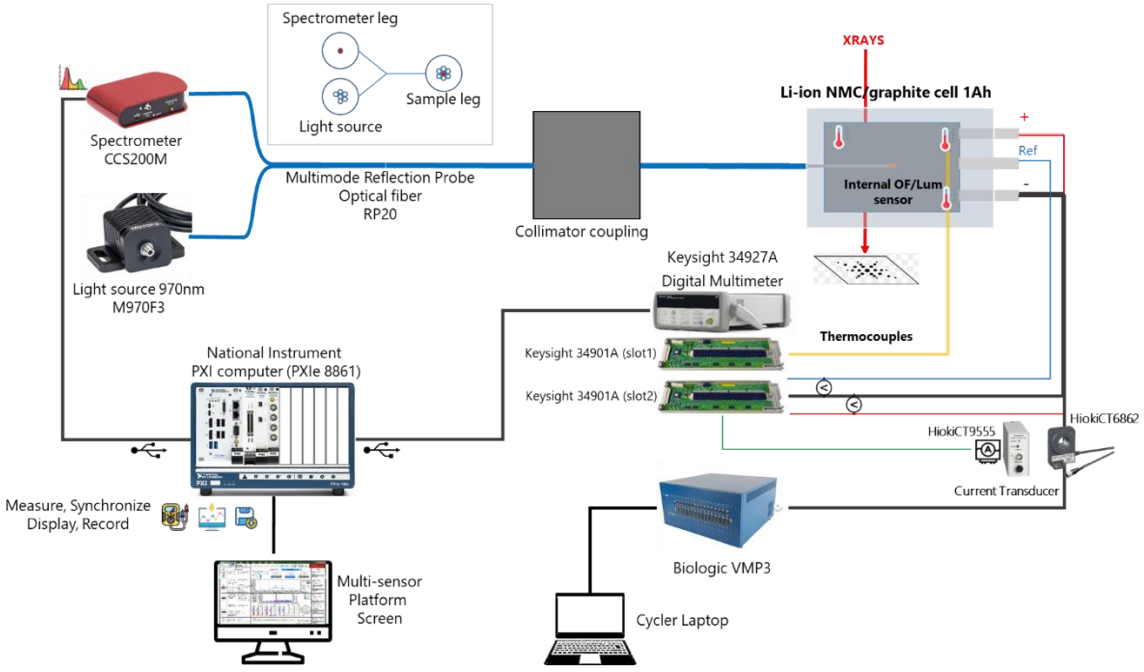

Figure S11. Schematic view of the experimental setup for the multi-layered cell (instrumented cell) monitoring.

Positions for data acquisition and external thermocouples: For the *operando* WAXS experiment, the multi-layered cell was additionally equipped with seven external thermocouples to monitor the external temperature of the cell at different locations: positive (TC04) and negative tap (TC02), at the center of the cell on both faces (TC06 and TC07), near the optical fiber (TC01) and the reference electrode (TC03).

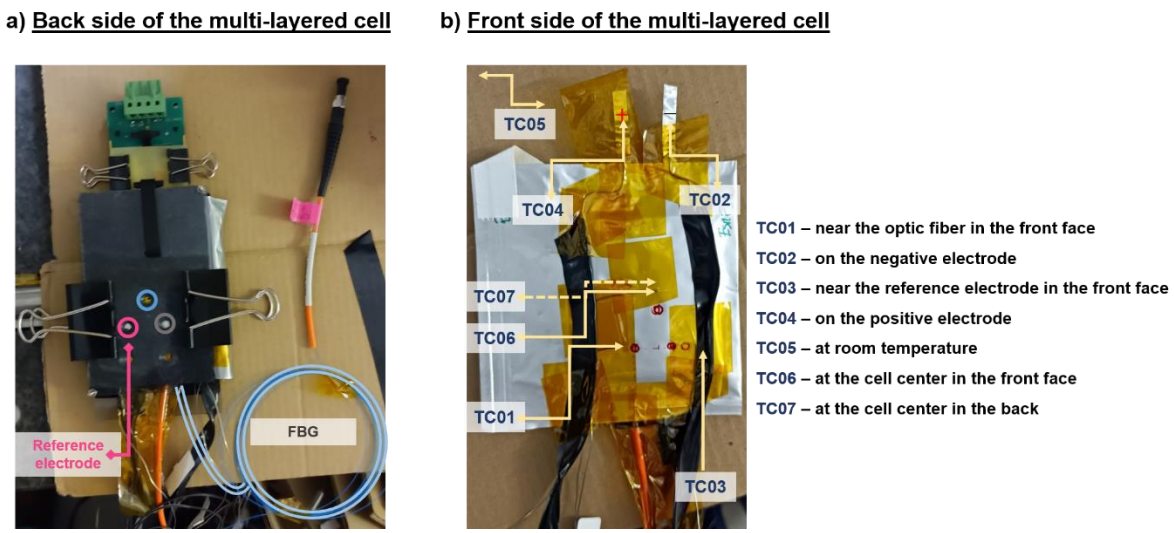

Figure S12. The setup of the multi-layered prismatic pouch cell equipped with the reference electrode, the optical fiber, and seven thermocouples (TC) for the *operando* WAXS measurement. (**a)** Back side of the multi-layered cell. Three holes with a diameter of 1 mm were drilled into the metal plate, one hole in the middle of the cell (blue), the second one near the reference electrode (pink), and the third one near the optical fiber (grey). (**b)** Front side of the multi-layered cell and the placement of thermocouples.

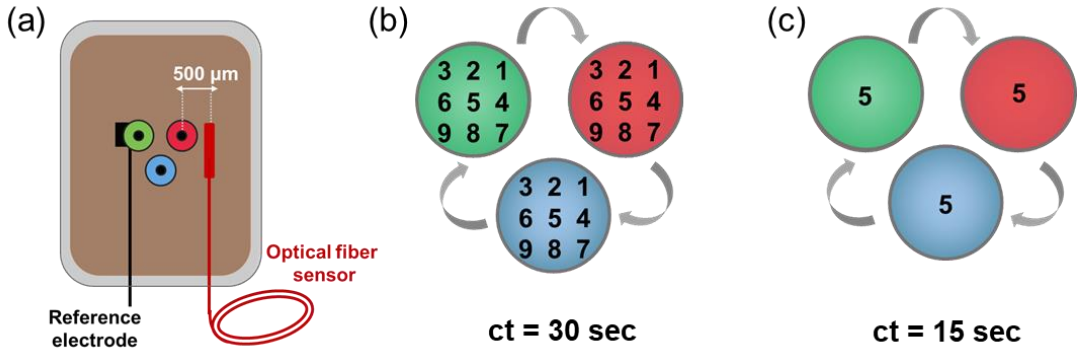

Figure S13. **(a)** Distances of the reference electrode and the optical fiber from the diffraction patterns collecting positions and scanning order between the holes **(b)** during 3x3 grid measurement and (**c)** while measuring the center of each hole in the multi-layered cell. Counting times per position (ct) range between 1 to 30 seconds depending on the type of measurement.

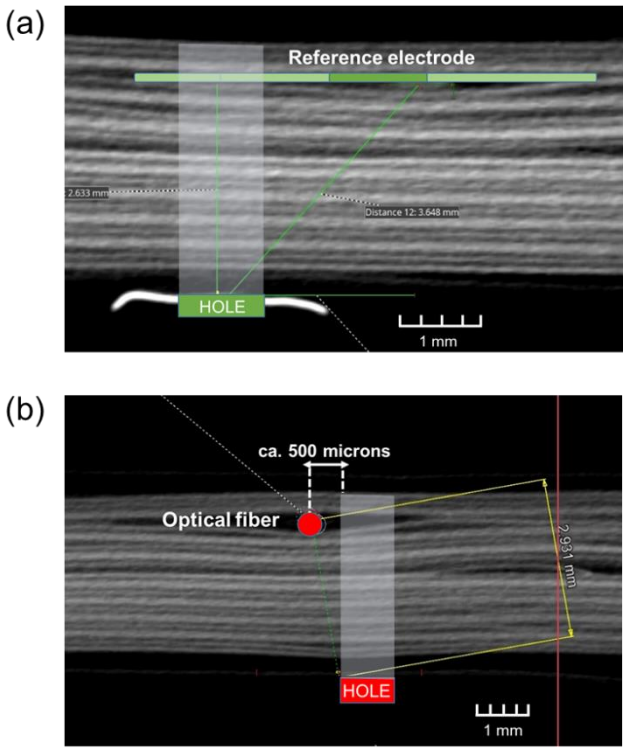

Figure S14. Distances of **(a)** the reference electrode and **(b)** the optical fiber from the diffraction collecting positions.

Multi-layered cell graphite lithiation kinetics in different positions: We observed that the insertion of the reference electrode did not disrupt lithiation kinetics in surrounding regions. In the delithiated state, a small additional peak at q = 1.805 $Å^{-1}$ was observed, which is coming from $LiFeO_4$ (LFP, the reference electrode material) (Fig. S13a), since the diffraction patterns were actually collected on the reference electrode. During the lithiation, there are small differences in peak shapes between the reference electrode location and the center of the cell. The differences were attributed to i) a 4.5 min time interval between these two measurements (corresponding to a 1.5% difference in SoC) (Fig. S15a–f) and ii) LFP peaks in this region. LFP peaks result in divergent peak shapes and intensities. Globally, we observe that the presence of the reference electrode appears to have a limited effect on the (de)lithiation kinetics in the region probed by the X-rays, indicating a negligible impact of the inserted object on the graphite staging mechanism.

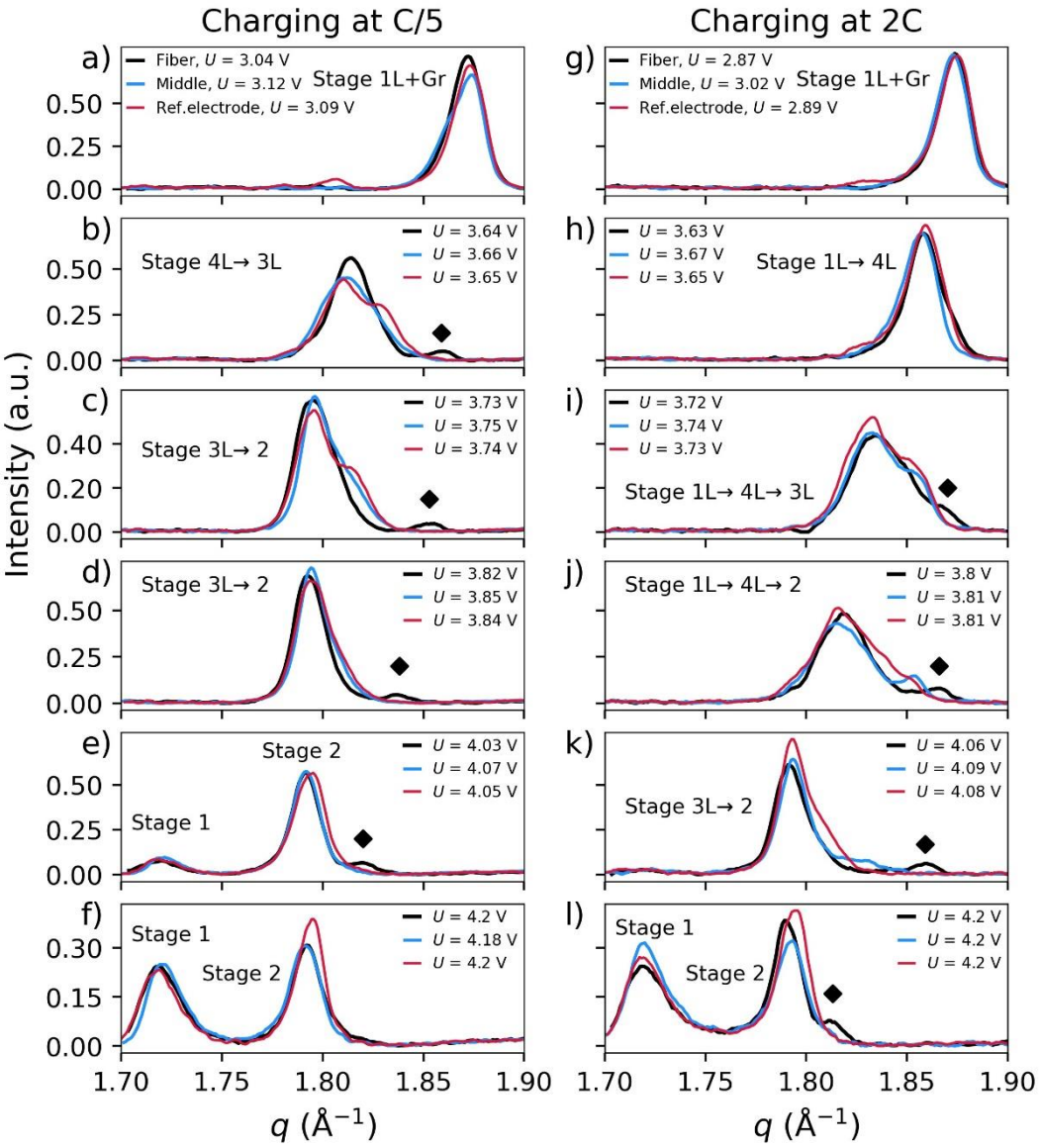

Figure S15. Diffraction patterns were collected near the reference electrode (red), middle of the cell (blue), and the optical fiber (black) during **(a–f)** charging at C/5, and **(g–l)** charging at 2C. Delayed graphite in the optical fiber diffraction patterns is marked with ♦.

References

1. Villemin, E. *et al.* Thermo-luminescent optical fibre sensor for Li-ion cell internal temperature monitoring. *J. Power Sources* **593**, 233981 (2024).
2. Dahn, J. R. Phase diagram of Li x C 6. *Phys. Rev. B* **44**, 9170–9177 (1991).
3. Konar, S., Häusserman, U. & Svensson, G. Intercalation Compounds from LiH and Graphite: Relative Stability of Metastable Stages and Thermodynamic Stability of Dilute Stage Id. *Chem. Mater.* **27**, 2566–2575 (2015).
4. Liu, Q. *et al.* Kinetically Determined Phase Transition from Stage II (LiC12) to Stage I (LiC6) in a Graphite Anode for Li-Ion Batteries. *J. Phys. Chem. Lett.* **9**, 5567–5573 (2018).
5. Didier, C., Pang, W. K., Guo, Z., Schmid, S. & Peterson, V. K. Phase Evolution and Intermittent Disorder in Electrochemically Lithiated Graphite Determined Using in Operando Neutron Diffraction. *Chem. Mater.* **32**, 2518–2531 (2020).
6. Taminato, S. *et al.* Real-time observations of lithium battery reactions—operando neutron diffraction analysis during practical operation. *Sci. Rep.* **6**, 28843 (2016).
7. Schmitt, C., Kube, A., Wagner, N. & Friedrich, K. A. Understanding the Influence of Temperature on Phase Evolution during Lithium-Graphite (De-)Intercalation Processes: An Operando X-ray Diffraction Study. *ChemElectroChem* **9**, e202101342 (2022).
8. Leach, A. S. *et al.* Spatially Resolved Operando Synchrotron-Based X-Ray Diffraction Measurements of Ni-Rich Cathodes for Li-Ion Batteries. *Front. Chem. Eng.* **3**, 794194 (2022).
9. Jousseaume, T., Colin, J.-F., Chandesris, M., Lyonnard, S. & Tardif, S. *How Beam Damage Can Skew Synchrotron Operando Studies of Batteries*. https://chemrxiv.org/engage/chemrxiv/article-details/63ca64de3e8656699689de43 (2023) doi:10.26434/chemrxiv-2023-rfp8j.